

A machine learning model to classify dynamic processes in liquid water

Jie Huang,¹ Gang Huang,² and Shibei Li¹

¹*Department of Physics, Wenzhou University, Wenzhou, Zhejiang 325035, China*

²*Institute of Theoretical Physics, Chinese Academy of Sciences, Beijing 100190, China*

(*Electronic mail: shibenli@wzu.edu.cn)

(*Electronic mail: hg08@lzu.edu.cn)

(Dated: 4 May 2022)

The dynamics of water molecules plays a vital role in understanding water. Up until now, we have mainly been studying the static properties of water. Nevertheless, if we want to understand water, we have to watch the water molecules in motion. We combined computer simulation and deep learning to study the dynamics of H-bonds between water molecules. Based on *ab initio* molecular dynamics simulations and a newly defined directed Hydrogen (H-) bond population operator, we studied a typical dynamic process in bulk water: donor-acceptor (DA) exchange, in which the H-bond donor reverses roles with the acceptor. By designing a recurrent neural network-based model, we have successfully classified the DA exchange and diffusion processes in water. We have found that the ratio between them is approximately 1:4, and it hardly depends on temperatures from 280 to 360 K. This work indicates that deep learning can help distinguish more complex dynamic processes in other systems like the water-vapor interface and electrolyte solutions.

I. INTRODUCTION

As one of the big questions in the 21st century¹, the structure of water is essential for understanding cells, biological processes, and ecosystems²⁻⁵. Water's surprising properties⁶⁻⁸, such as increased density on melting, high surface tension, maximum density at 4 °C, are closely related to the H-bond dynamics in water⁹⁻¹¹. However, few experimental studies can provide a molecular-level understanding of the dynamic properties of water¹², as it is tough to capture the ultrafast motion of atoms during dynamic processes¹³. Until now, we have mainly been studying the static properties of water. Nevertheless, watching water molecules as they dance is the key to understand water¹⁴. Many methods can be used to study water molecules' motion, such as scanning tunneling microscopy (STM)^{15,16}, infrared (IR) spectroscopy^{13,17-19}, X-rays^{14,20,21}, neutron scattering²², and computer simulations^{9,23-25}.

In this work, we focus on one specific dynamic process in bulk water: the donor-acceptor (DA) exchange, in which the H-bond donor reverses roles with the acceptor in the same H-bond. The DA exchange process, which involves the quantum tunneling effect^{16,23,25-27}, is essential for understanding water molecules' dynamics. Also, since DA exchange processes are closely related to the H-bond network dynamics, it is likely to play a critical role in biological processes, like proton transfer²⁸⁻³⁰. So far, DA exchange processes have been found in water dimer adsorbed on metal surfaces¹⁶. Using *ab initio* molecular dynamics (AIMD) simulations³¹, Ranea et al.²³ found that the DA exchange can be used to explain the rapid diffusion behavior of water dimer on the Pd(111) surface. Fang et al.²⁵ found that DA exchange is a mechanism of the rapid movement of water dimers on metal surfaces. As for bulk water, Lagge and Hynes found that the redirection of water molecules involves large-angle jumps²⁴, which involves the redirection of *multiple* water molecules referred to as *H-bond exchange*, and it is supported by the subsequent experiments^{32,33}.

Although there are some simulation studies on the DA exchange process in water clusters^{26,27,34,35}, as far as we know, the question of the ratio of DA exchange to other dynamic processes related to H-bonds has not been discussed. To answer this question, we simulated bulk water in a canonical (NVT) ensemble using a specific AIMD simulation method: the density functional molecular dynamics (DFTMD) simulation. We observed DA exchange processes in bulk water by analyzing the dynamic trajectory.

As it's tough to determine the proportion of DA exchange processes in a large number of ultrafast dynamic processes in liquid water, we have designed a recurrent neural network (RNN)-based model to classify the H-bond dynamic processes. Unlike general classification methods, this model has the capability of classifying the *dynamic processes* related to H-bonds in bulk water. Using this model, we have obtained the relative ratio of DA exchange and diffusion processes in bulk water and explored the effect of temperature on this ratio. Our work presents the great capacity to use the RNN-based deep learning method to study the dynamic properties of liquid water.

The organization of the paper is the following. We present the results and discussion in Sec. II. At first, the dynamic graph representation of H-bond networks is introduced in II A and the main characteristics of DA exchange processes are obtained in II B. Then we implement the RNN-based classifier for different types of dynamic processes in liquid water in II C and explore the temperature dependence of the relative ratios of DA exchange and diffusion processes in II D; The discussion of two factors, the mean number of H-bonds and the rate of breakage and formation of H-bonds in liquid water, related closely to the temperature dependence are discussed in II E. The validation calculations in II F and II G are used to support our results. Finally, we present the conclusions of our study and methods details in Sec. III and IV, respectively.

II. RESULTS AND DISCUSSION

A. Dynamic graph representation of H-bond networks

As shown in Fig. 1, a directed *dynamic* graph is used to describe the bulk water system of N water molecules. Each water molecule may form an H-bond with any of the remaining $N-1$ molecules. For convenience, we call any pair of water molecules (i, j) a *quasi-hydrogen bond* (Q-bond), denoted as QB_{ij} and represented as a dashed line in Fig. 1.

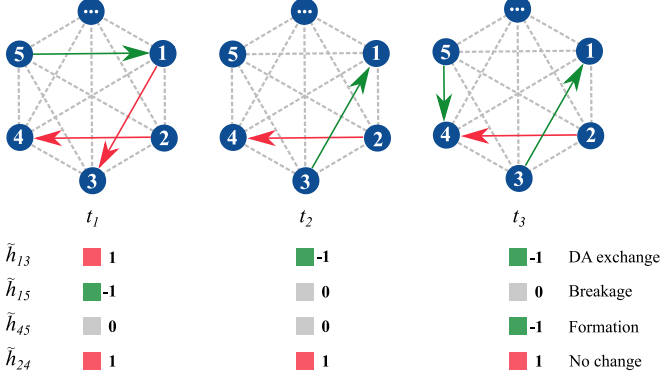


FIG. 1. Dynamic graph representation of the H-bond network in simulated bulk water. Nodes represent water molecules; solid red or green arrows represent H-bonds; and dashed grey lines represent Q-bonds. The colors red, grey, and green indicate $\tilde{h}_{ij}=1$, $\tilde{h}_{ij}=0$, and $\tilde{h}_{ij}=-1$, respectively. From the time sequence of \tilde{h}_{ij} , we know how the H-bond configuration of QB_{ij} changes over time. Four typical H-bond configuration change processes are illustrated for QB_{13} , QB_{15} , QB_{45} , and QB_{24} , corresponding to DA exchange, breakage, formation, and no change, respectively.

Inspired by Luzar and Chandler's H-bond population operator¹², we define a *directed* H-bond population operator \tilde{h}_{ij} for QB_{ij} ($i < j$) at time t as Eq. 1.

$$\tilde{h}_{ij}(t) = \begin{cases} 1 & \text{H-bonded, } i \text{ is the donor} \\ 0 & \text{Not H-bonded} \\ -1 & \text{H-bonded, } j \text{ is the donor} \end{cases} \quad (1)$$

We know from \tilde{h}_{ij} whether an H-bond exists in QB_{ij} and the donor-acceptor pair of the formed H-bond. At the bottom of Fig. 1, we demonstrate four typical H-bond configuration change processes by using the sequences of \tilde{h} : DA exchange, breakage, formation, and no change. Besides, the Q-bonds likely to form H-bonds are the most relevant water molecule pairs to the breakage and reforming of H-bond networks. The following geometric criteria³⁶⁻³⁸ of an H-bond is used: O-O distance $R_{OO'} < R_{\text{cutoff}} = 3.5 \text{ \AA}$ and angle $\text{O-H} \cdots \text{O} > \theta_{\text{cutoff}} = 120^\circ$. As shown in Fig. 2, $R_{OO'}$, θ_a , θ_b , θ_c , and θ_d are monitored for Q-bonds to study the reorientation and diffusion mechanism of H-bonds.

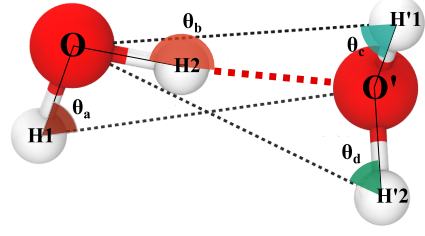


FIG. 2. Scheme of the geometric coordinates. $R_{OO'}$ is the O-O distance. Four angles $\widehat{\text{OH1O'}}$, $\widehat{\text{OH2O'}}$, $\widehat{\text{O'H'1O}}$, and $\widehat{\text{O'H'2O}}$ are represented as θ_a , θ_b , θ_c , and θ_d , respectively. If $R_{OO'} < 3.5 \text{ \AA}$, and any angle $\theta > 120^\circ$ ($\theta \in \{\theta_a, \theta_b, \theta_c, \theta_d\}$), then an H-bond exists in this Q-bond. Here, the oxygen atom O as a donor donates the hydrogen atom H2 to the acceptor O'. Since $R_{OO'} < 3.5 \text{ \AA}$ and $\theta_b > 120^\circ$, we describe this state of $QB_{OO'}$ at this time t by $\tilde{h}_{OO'}(t) = 1$.

B. Donor-acceptor exchange process

The AIMD simulation trajectory allows us to observe the details of the H-bond dynamics. Figure 3 demonstrates the dynamics of the distance, angles, and directed H-bond population for $QB_{OO'}$. Intervals I_1 , I_2 , and I_3 correspond to three typical H-bond dynamic processes. *DA exchange* (I_1): We notice $\theta_b > \theta_{\text{cutoff}}$ in the first half and $\theta_d > \theta_{\text{cutoff}}$ in the second half. Besides, $\tilde{h}_{OO'}$ changes from 1 to -1 , indicating that the donor and acceptor have exchanged. *Translational diffusion* (I_2): $\tilde{h}_{OO'} = -1$ in the first half of I_2 , and $\tilde{h}_{OO'} = 0$ for most of the second half. There is no H-bond in the second half because $R_{OO'} > R_{\text{cutoff}}$, i.e., the increase of distance $R_{OO'}$ causes the H-bond to break. *HH exchange* (I_3): At first, the hydrogen atom H'1 is donated to form an H-bond as $\theta_c > \theta_{\text{cutoff}}$. Then θ_c decreases and θ_d increases until $\theta_d > \theta_{\text{cutoff}}$, i.e., the other hydrogen atom H'2 of the donor is donated to form the H-bond. Therefore, the hydrogen atom contributed by the donor is changed. Because of the identity of hydrogen atoms, it is impossible to distinguish the configuration of water molecules before and after the HH exchange. However, during the DA exchange process, the direction of the water molecules' dipole moment will change, indicating that the water molecules' microscopic configuration will change. So in the rest of the article, we focus on the DA exchange process.

Figure 4 shows a typical DA exchange process in water (see Fig. 14 in Appendix A and movies in supplementary material for more H-bond configuration change processes). A dashed line represents an H-bond, and its color (red or green) indicates its direction. Using \tilde{h} , we can describe the H-bond configuration change progress without paying attention to the distance and angles. Therefore, \tilde{h} dramatically simplifies the description for the H-bond configuration change process. Nevertheless, during dynamic processes, the value of \tilde{h} would fluctuate due to the vibration of water molecules, which will bring a huge challenge for the classification of H-bond configuration change processes. In addition, due to a large number of Q-bonds in the simulated bulk water, finding a specific H-bond configuration change process in 60 ps is like finding a needle in a haystack. Therefore, we design an RNN-based model that

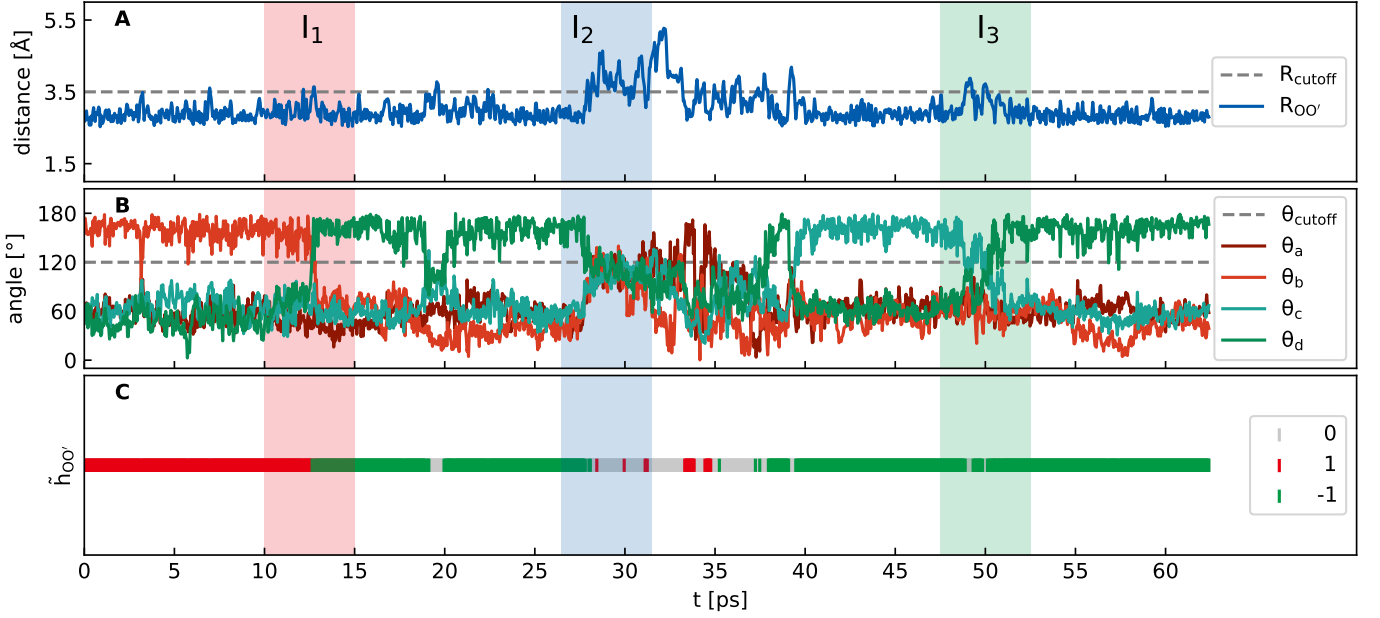


FIG. 3. DA exchange (I_1), diffusion (I_2), and HH exchange (I_3) process for one typical Q-bond in bulk water. When an H-bond exists in a Q-bond if $\theta_a > \theta_{\text{cutoff}}$ or $\theta_b > \theta_{\text{cutoff}}$, then the oxygen atom O is the donor; else, if $\theta_c > \theta_{\text{cutoff}}$ or $\theta_d > \theta_{\text{cutoff}}$, then the oxygen atom O' is the donor. Three typical processes are DA exchange, where the water molecule pairs exchange their roles as H-bond donor and acceptor; diffusion, where the H-bond is breaking as the distance increase of this water molecule pair; and HH exchange, where the donated hydrogen atom of the H-bond donor exchanged. Through \tilde{h} , we can see whether an H-bond exists between a Q-bond, also know the donor and acceptor if an H-bond exists. In panel (C), the grey, red, and green lines indicate the $\tilde{h}_{OO'}$ states.

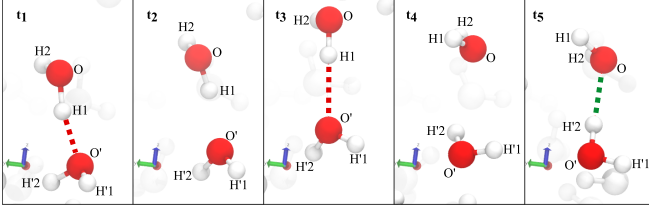


FIG. 4. A typical DA exchange process, where two water molecules exchange their roles as H-bond donor and acceptor via water molecules' reorientation in an concerted manner. The donor oxygen atom has changed from the original O to O' (color of dashed line changed from red to green). Besides, we have also noticed that the H-bond briefly breaks during the DA exchange process, causing the fluctuation of the \tilde{h} sequence.

recognizes the dynamic processes related to H-bonds and uses it to determine various processes in water, thereby determining the ratio of DA exchanges.

C. RNN-based classifier for H-bond configuration change process

We can see the DA exchange and diffusion processes intuitively from \tilde{h} . Specifically, in the DA exchange process, \tilde{h} changes from ± 1 to ∓ 1 ; in the diffusion process, \tilde{h} changes from ± 1 to 0. Therefore, in principle, by observing the sequence of \tilde{h} within a time window, we can classify the H-

bond configuration changes during this period. Although we can see some change patterns in DA exchange and diffusion processes, it is still challenging to distinguish different \tilde{h} sequences due to the fluctuation. Therefore, we have designed a processing flow to classify the H-bond configuration change process based on RNN, as shown in Fig. 5. In the preprocessor, we use a low-pass filter to filter out the high-frequency fluctuations of \tilde{h} sequences. As we focus on the configuration change processes of H-bonds, we exclude sequences without H-bonds at the beginning (T_1) and the sequences whose H-bond configuration are unchanged (T_2, T_3) according to the initial value and the variance of \tilde{h} sequences (see Methods section). After preprocessing, the task we need to deal with is a time series classification problem: In addition to DA exchange and diffusion processes, there are also many irregular and complicated processes. We call the sequences of DA exchange and diffusion *positive* and all sequences other than these two types *negative* for convenience. Negative sequences (T_4) do not have any particular pattern. We do not expect that general supervised learning can be used to distinguish them. Nevertheless, we can teach a machine to learn to *recognize* positive sequences. Due to the need to classify time series, we use a typical method for modeling ordered data^{39–41}, recurrent neural network (RNN)^{42,43}. Specifically, we have designed a bidirectional long short-term memory (BLSTM) autoencoder (AE), whose goal is to reconstruct the input sequences as much as possible. We have trained this AE using positive sequences only and evaluated how well the AE reconstructs for an input sequence \mathbf{x} using reconstruction error $\mathcal{L}(\mathbf{x})$ (see

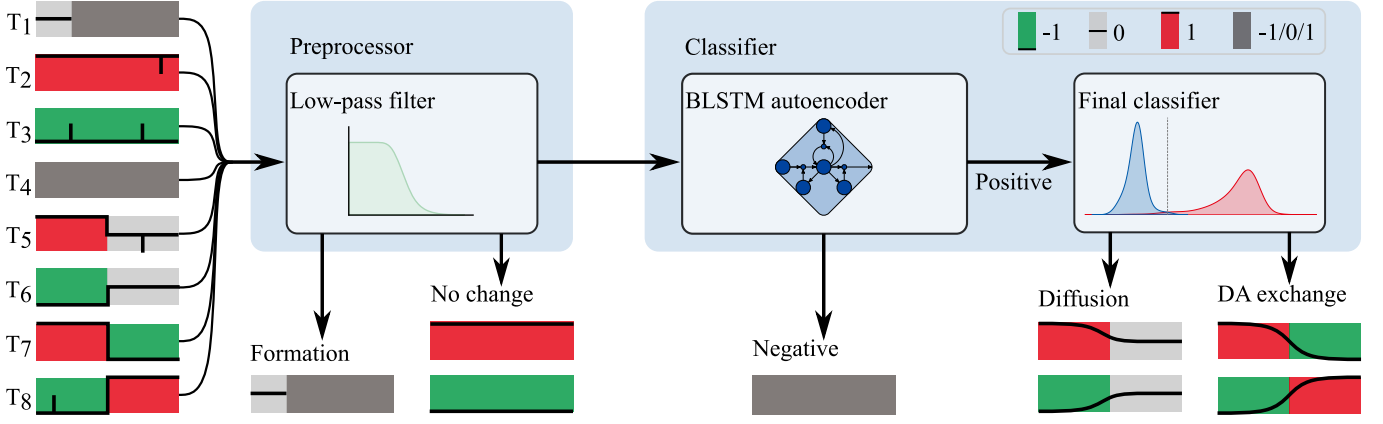


FIG. 5. The processing flow of the H-bond configuration change classifier based on RNN. (i). Different types of \tilde{h} sequences: T₁: Formation or no H-bond; T₂, T₃: No change; T₄: Negative sequence; T₅, T₆: Diffusion; T₇, T₈: DA exchange. We refer to the sequences of diffusion and DA exchange as positive sequences. (ii). The preprocessor filters out the high-frequency components of \tilde{h} and excludes T₁, T₂, and T₃. (iii). The classifier consists of a BLSTM AE to separate the positive and negative sequences and a final classifier to distinguish diffusion and DA exchange sequences.

Methods Section IV D, Eq. 7). After training, the autoencoder can reconstruct positive processes very well. However, when we input negative sequences into the AE, likely, it would not be able to reconstruct them well, leading to the reconstruction errors of these negative sequences greater than that of the positive sequences. Through the reconstruction error, we can determine whether a \tilde{h} sequence is positive or negative. Fi-

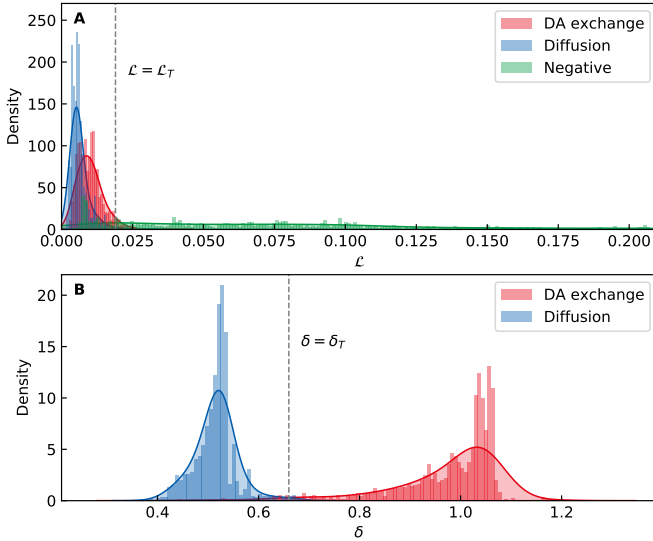


FIG. 6. (A) Densities of reconstruction error \mathcal{L} for DA exchange, diffusion, and negative sequences. (i) BLSTM AE can reconstruct positive sequences well. Hence, the reconstruction errors for DA exchange and diffusion sequences are relatively small, mainly less than \mathcal{L}_T . (ii) Since negative sequences are not used to train BLSTM AE, it is much more difficult for the autoencoder to reconstruct them. Therefore, the reconstruction errors are relatively large, mainly greater than \mathcal{L}_T . (iii) Once \mathcal{L}_T is determined, we use it as the threshold to distinguish positive and negative sequences. (B) Densities of the range δ for DA exchange and diffusion sequences. The two densities are significantly different from each other.

nally, we use a *final classifier* to distinguish sequences between DA exchange and diffusion processes from positive sequences. We use the range of a positive sequence \mathbf{x} to determine whether it is DA exchange or diffusion, which is defined as $\delta(\mathbf{x}) = \max \mathbf{x} - \min \mathbf{x}$.

Figure 6 (A) shows the densities of the reconstruction errors for DA exchange, diffusion, and negative sequences. Since BLSTM AE can reconstruct positive sequences well, the reconstruction errors of DA exchange and diffusion sequences are small, most of which are smaller than the reconstruction error threshold \mathcal{L}_T (\mathcal{L}_T is determined in Methods Section IV D, Fig. 13). Negative sequences are not used to train the autoencoder, so it is much more difficult to reconstruct them. Hence, the reconstruction errors are relatively large, most of which are greater than \mathcal{L}_T . As long as we find a suitable reconstruction error threshold, we can get a classifier for positive and negative sequences. Figure 6 (B) shows the densities for the range of normalized DA exchange and diffusion sequences. The two distributions are significantly different from each other. Therefore, the final classifier can distinguish DA exchange and diffusion sequences very well via $\delta_T = 0.66$, as shown in the dashed line (see the classification process in Appendix A, Fig. 14-15). Therefore, we have obtained an H-bond configuration change classifier based on an RNN autoencoder.

D. Proportions of DA exchange at different temperatures

To explore the effect of temperature on the H-bond configuration change process, we have simulated nine bulk water systems containing $N = 64$ water molecules. The temperature ranges from 280 to 360 K every 10 K. Using the RNN-based model, we classify \tilde{h} sequence, count the number of DA exchange and diffusion sequences at each temperature. As shown in Fig. 7, the number of DA exchange and diffusion processes shows a "rising first, then decreasing" trend as the

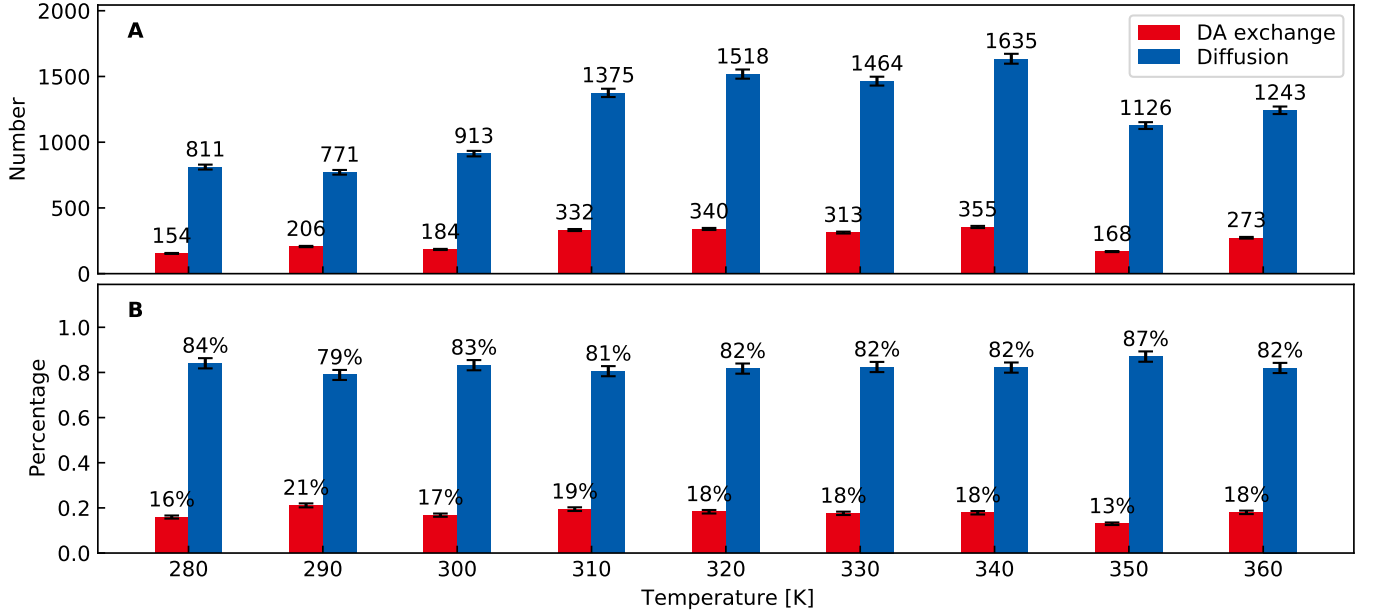


FIG. 7. The number (A) and proportion (B) of DA exchange and diffusion processes determined by the RNN-based classifier at different temperatures. (i) With the temperature increasing, the number of DA exchange and diffusion processes increases first and then decreases on the whole. (ii) The relative ratio of DA exchange to diffusion basically does not depend on temperature.

temperature increases. In other words, there is an overall upward trend from 280 to 330 K. However, as the temperature continues to rise, the number of DA exchange and diffusion processes tends to decrease. On the other hand, although the number of DA exchange and diffusion processes vary at different temperatures, the relative ratios between the two are almost unchanged, which is still about 1:4. This result indicates that the relative ratio is almost not dependent on temperature, and the DA exchange process is another important mechanism in bulk water besides the diffusion process. Next, we will explain this trend of the number of DA exchange and diffusion processes from the following two aspects: the number of H-bond per molecule and the change rate of the coarse-grained H-bond network configuration.

E. The trend of DA exchange and diffusion process number

To understand the trend in Fig. 7 (A), we first calculate the number of H-bonds per molecule (n_{HB}) in the simulated system. At time t , n_{HB} can be expressed as Eq. 2,

$$n_{HB}(t) = \frac{2}{N} \sum_{i=1}^N \sum_{j>i}^N |\tilde{h}_{ij}(t)| \quad (2)$$

where $N = 64$ is the number of water molecules in bulk water systems, and $|\tilde{h}_{ij}(t)|$ is the absolute value of $\tilde{h}_{ij}(t)$, i.e., the H-bond direction is ignored. The factor 2 is derived from the fact that one H-bond in water is shared by two water molecules. For a certain trajectory at one temperature, by counting n_{HB} at each time t , we get the distribution of n_{HB} (one density plot in Fig. 8 A). Then we use an L -dimensional vector $\tilde{\mathbf{h}}(t)$

to represent the coarse-grained H-bond network *configuration* for the simulated bulk water system at time t in Eq. 3,

$$\tilde{\mathbf{h}}(t) = (\tilde{h}_{12}(t), \tilde{h}_{13}(t), \dots, \tilde{h}_{ij}(t), \dots, \tilde{h}_{N-1,N}(t)) \quad (3)$$

where $L = N(N-1)/2$ is the number of Q-bonds in the system. So in a unit time, we get a set H of $\tilde{\mathbf{h}}(t)$ in Eq. 4,

$$H = \{\tilde{\mathbf{h}}(t) \mid t = t_0 + k\Delta t, k = 0, 1, \dots, M\} \quad (4)$$

where t_0 represents the start time of the unit time window, Δt is the time interval between two adjacent frames, and M is the length of the unit time window. In a unit time $t_w = M\Delta t$, the number of graph configuration can be expressed as $\Omega = |H|$, where $|H|$ is the size of the set H , i.e., the number of different $\tilde{\mathbf{h}}$ vectors in this unit time. The number Ω of graph configuration per unit time characterizes the *rate* of breakage and reforming of the H-bonds in bulk water. The theoretical upper bound of Ω in t_w is $M+1$; in this case, all $\tilde{\mathbf{h}}$ vectors are different. By changing the start point t_0 , we get the distribution of Ω .

Figure 8 shows the temperature dependence of the distributions of n_{HB} and $\ln \Omega$. The width of a density plot indicates the probability of n_{HB} or $\ln \Omega$ at the corresponding temperature. From the medians (white dots) of violin plots in Fig. 8 (B), we see Ω is relatively smaller at lower temperatures, indicating fewer changes of H-bond configuration in the unit time. This result explains why the number of DA exchange and diffusion processes at lower temperatures in Fig. 7 (A) are smaller. Besides, the direct reason for the decrease in the number of DA exchange and diffusion processes at higher temperatures is that n_{HB} decreases with increasing temperature. Therefore, the number of DA exchange and diffusion processes in Fig. 7 (A) is determined by n_{HB} and Ω together.

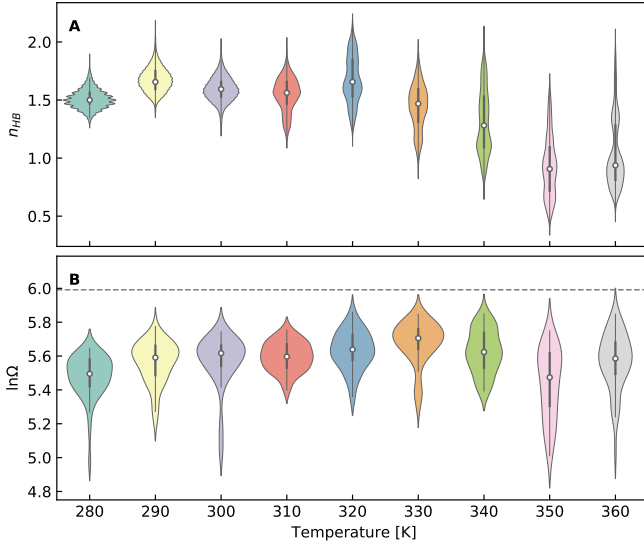


FIG. 8. The temperature dependence of (A) The distributions of the number n_{HB} of H-bonds per molecule. (B) The distributions of $\ln \Omega$ characterizing the rate of H-bond breakage and reforming. The dashed line denotes the upper bound of $\ln \Omega$ in the unit time of 1 ps.

F. The number of H-bonds per molecule and H-bond relaxation time.

The choices of different H-bond definitions may affect the relative ratio of DA exchange and diffusion processes. Based on two different H-bond definitions, we calculate the average number $\langle n_{\text{HB}} \rangle$ of H-bonds per molecule and H-bond relaxation time τ_{R} . The average number $\langle n_{\text{HB}} \rangle$ of H-bonds in bulk water of N water molecules is $\frac{1}{2}N(N-1)\langle h \rangle$, where $\langle h \rangle$ denotes the average of Luzar-Chandler's H-bond population operator h^{12} . The τ_{R} is computed by⁴⁴

$$\tau_{\text{R}} = \frac{\int t C_{\text{HB}}(t) dt}{\int C_{\text{HB}}(t) dt} \quad (5)$$

where $C_{\text{HB}}(t) = \langle h(0)h(t) \rangle / \langle h \rangle$ is the autocorrelation of h . The difference between the two H-bond definitions lies in the different geometric conditions, which are as follows. Definition 1: $R_{\text{OO}'} < 3.5 \text{ \AA}$, $\widehat{\text{OHO}'} > 120^\circ$; Definition 2: $R_{\text{OO}'} < 3.5 \text{ \AA}$, $\widehat{\text{HOO}'} < 30^\circ$.

Figure 9 (A) shows the temperature dependence of $\langle n_{\text{HB}} \rangle$ under two different geometric H-bond definitions. For both definitions, the $\langle n_{\text{HB}} \rangle$ shows a downward trend as the temperature increases. In general, the $\langle \tau_{\text{R}} \rangle$ also decreases as the temperature increases for both geometric definitions. Figure 9 shows that the different definitions of H-bond may cause some differences in observations. However, the relationship of $\langle n_{\text{HB}} \rangle$ and τ_{R} with temperature changes is consistent. We can understand this similarity as follows. Shorter H-bond relaxation time at higher temperatures means that each water molecule has fewer H-bonds on average. Under different H-bond definitions, we have found that the changing trends of the mean number of H-bonds and relaxation time of H-bonds would not change with the H-bond definition.

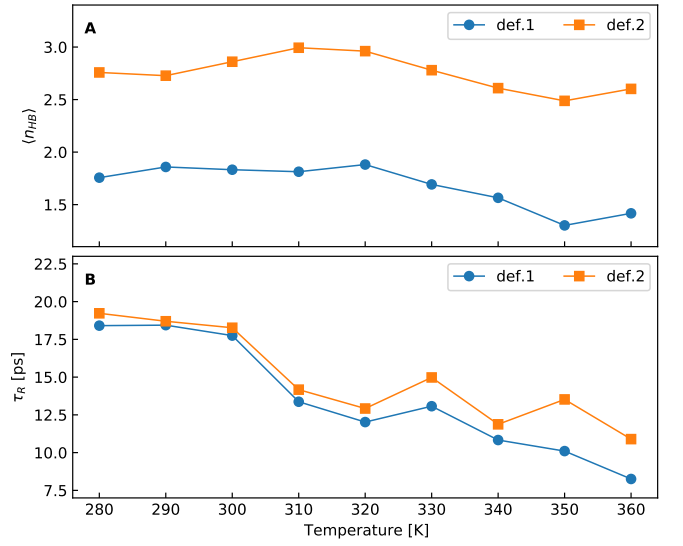


FIG. 9. (A) Mean number $\langle n_{\text{HB}} \rangle$ of H-bonds per water. (B) Relaxation time τ_{R} of H-bonds. Both $\langle n_{\text{HB}} \rangle$ and τ_{R} are calculated for two geometric definitions.

G. Velocity autocorrelation function and vibrational density of states

In this work, we have simulated bulk water in a large temperature range by using DFTMD with DFTD3 correction. To prove that dynamic properties are evaluated with accuracy, we calculate the velocity autocorrelation function (VACF) and its Fourier transform, the vibrational density of states (VDOS) of the water molecules in the simulated bulk water systems. For a system containing M atoms, the VACF $C(t)$ can be expressed as

$$C(t) = \frac{\langle \sum_{i=1}^M \mathbf{v}_i(t) \cdot \mathbf{v}_i(0) \rangle}{\langle \sum_{i=1}^M \mathbf{v}_i(0) \cdot \mathbf{v}_i(0) \rangle} \quad (6)$$

where $\langle \dots \rangle$ represents the averaging over all the time starting points, t is the time interval, and \mathbf{v}_i represents the velocity of the i -th atom. Figures 10 (A) and (B) show the VACF and VDOS of bulk water systems at different temperatures, respectively. The VDOS we obtained is in good agreement with previous experiments and *ab initio* all-electron calculations^{45,46}, which laid a foundation for us to observe the motion of water molecules from the microscopic level.

To display the information of OH stretching more clearly, we made Fig. 10 (B2), just zooming in on the third band in Fig. 10 (B1). The position of the third peak represents the OH stretching vibration frequency of water molecules. From Fig. 10 (B2), we can see that with the increase of temperature, the peaks of OH stretching bands are blue-shifted. This result means that the increasing temperature causes a higher frequency of OH stretching. As OH stretch frequency is correlated to the strength of H-bonds in which the OH bonds are involved^{47,48}, the blue-shifted OH stretch band has been assigned to weakly H-bonded water. Therefore, both the shorter relaxation time τ_{R} and blue-shifted OH stretch frequency are

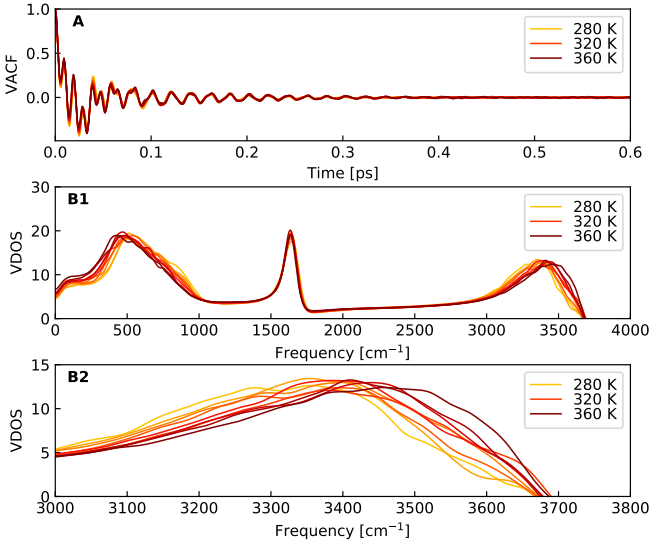


FIG. 10. Velocity autocorrelation function (A) and vibrational density (B) of states.

consistent with the smaller $\langle n_{HB} \rangle$ as temperature increases.

III. SUMMARY

In summary, we have designed and trained a deep learning-based model to recognize different types of processes related to H-bonds. The priority of this model is its remarkable ability to classify different dynamic processes of water molecules. Using this model, we have found that the relative ratio of DA exchange and diffusion processes is approximately 1:4, and this ratio hardly depends on temperature. We have explained the reason behind the number of DA exchange and diffusion processes under different temperatures and found the number of DA exchange processes is related closely to the number of H-bonds and the rate of breakage and reforming of H-bonds.

Moreover, the key concepts used in this work are the dynamic graph and the newly defined directed H-bond population. This reasonable coarse-grained description of the H-bond network simplifies the analysis of H-bond dynamics dramatically. This work demonstrates that the semi-supervised RNN-based model has an outstanding capability of classifying the dynamic processes related to H-bonds in bulk water, which implies the great potential to extend our present scheme to distinguish more complex dynamic processes in other systems like the water-vapor interface and electrolyte solutions.

IV. METHODS SECTION

A. AIMD simulations

AIMD simulations were carried out for bulk water of 64 water molecules within the canonical NVT ensemble using CP2K/QUICKSTEP (v7.1)⁴⁹. The number N of water

molecules was 64 for all bulk water systems at different temperatures from 280 to 360 K. The length of the periodic cubic box was 12.4295 Å. The discretized integration time step Δt was set to 0.5 fs. The simulation time was 60 ps. The BLYP functional, which consists of Becke non-local exchange⁵⁰ and Lee-Yang-Parr correlation⁵¹, was used; Interactions between the valence electrons and the ionic cores were described by GTH pseudopotentials^{52,53}; Valence electrons were expanded in a basis set consisting of double-zeta Gaussian functions⁵⁴ and plane waves with a cutoff energy of 280 Ry⁴⁹. The Nosé-Hoover chain thermostat⁵⁵ was used to conserve temperature. DFT-D3 correction⁵⁶ for the dispersion interaction was used to obtain an accurate description of the vibrational properties.

B. Trajectory analysis

MDAnalysis (v1.0.0)³⁸ is used to analyze the simulation trajectories. The first 10 ps non-equilibrium trajectory is removed, and the remaining 50 ps trajectory is sampled every 80 frames. So the time interval after sampling is $80\Delta t = 40$ fs. Next, we use the HydrogenBondAnalysis module to find the atom IDs of the H-bond donor, acceptor, and the contributed hydrogen in each frame used to model the dynamic graph.

C. Sequence collection and preprocessing

The sequence length of \tilde{h} was 200 corresponding to 8 ps simulation time. Positive sequences in which only one DA exchange or diffusion process occurred were collected. Negative \tilde{h} sequences used to evaluate the BLSTM AE classifier were also collected. BLSTM AE was trained by 6786 positive sequences, of which the DA exchange and diffusion processes each accounted for half (754 positive sequences at each temperature). There were 18,931 negative sequences for evaluating the BLSTM AE classifier. The filtered sequence $\tilde{h}_f[n]$ was obtained by second-order Butterworth filter implemented by Scipy⁵⁷. In addition, if $\tilde{h}_f[0] - 0.5 < 0.15$, indicating no H-bond at the beginning (T_1). If the standard deviation σ of $\tilde{h}_f[n]$ satisfy $\sigma < 0.1$, then we consider the H-bond configuration in the Q-bond has not changed (T_2, T_3).

D. Bidirectional LSTM autoencoder classifier

The encoder and the decoder of BLSTM AE can be expressed as two transformations, $\phi: \mathcal{X} \rightarrow \mathcal{F}$ and $\psi: \mathcal{F} \rightarrow \mathcal{X}$, where \mathcal{X} and \mathcal{F} are the input space and the feature space, respectively. The dimension of \mathcal{F} is smaller than that of \mathcal{X} , and the feature vector $\phi(\mathbf{x})$ is the compressed representation of input \mathbf{x} . The input \mathbf{x} of BLSTM AE is the normalized and filtered directed H-bond population operator sequence $\tilde{h}_f[n]$. The reconstruction error of BLSTM AE for a sequence $\mathbf{x} = \tilde{h}_f[n]$ is defined as

$$\mathcal{L}_{\omega, \omega'}(\mathbf{x}) = \|\mathbf{x} - \psi_{\omega'}(\phi_{\omega}(\mathbf{x}))\|^2 \quad (7)$$

where ω, ω' represent the parameters of the encoder and decoder respectively. The purpose of training is to obtain the optimal ω, ω' ,

$$\omega^*, \omega'^* = \arg \min_{\omega, \omega'} \frac{1}{m} \sum_{i=1}^m \mathcal{L}_{\omega, \omega'}(\mathbf{x}^i) \quad (8)$$

where \mathbf{x}^i represents the i -th sequence.

LSTM is a type of RNN architecture specifically designed to solve the vanishing gradient problem of standard RNNs. It can learn to model time intervals over 1000 steps even in noisy input sequences without losing short time lag capabilities⁴³. The LSTM hidden layer is composed of recurrently connected memory blocks. Each block contains a group of internal units whose activation is controlled by three multiplication gates: input gate, forget gate, and output gate⁵⁸. Figure 11 shows a LSTM memory block with a single unit in detail. For

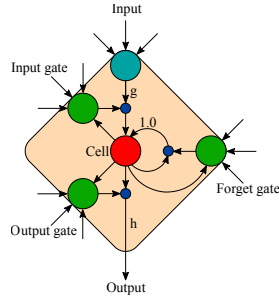


FIG. 11. LSTM unit. The outcome of the gates is to allow the cell to store and access information over long periods⁵⁸.

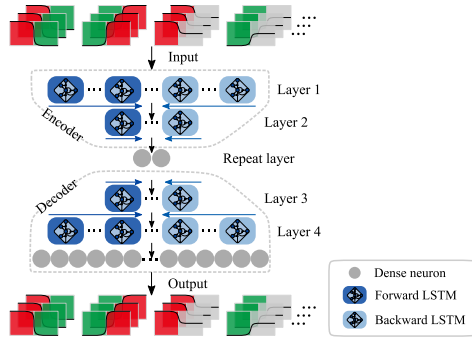


FIG. 12. The structure of BLSTM AE. This kind of design is used to identify positive and negative \tilde{h} sequences. The training data for the BLSTM AE are the filtered positive \tilde{h} sequences. Since \tilde{h} sequences are time-varying sequences, we choose to use the LSTM unit as the building block. The \tilde{h} sequence's start and end are equally crucial for the classification, so we use a bidirectional network structure.

the classification of H-bond configuration change processes, it is useful to access future and past contexts. Bidirectional RNNs^{59,60} can access contextual information in two directions along the input sequence. BRNNs contain two independent hidden layers; one hidden layer processes the forward input sequence, and the other hidden layer processes the reverse sequence. Both hidden layers are connected to the same output

layer to access the past and future information of each point in the sequence. Combining BRNNs, LSTM, and autoencoder gives bidirectional LSTM autoencoder (BLSTM AE) as shown in Fig. 12. The BLSTM AE is implemented using the Keras module of Tensorflow (2.2.0). Layer 1 contains two LSTM layers, forward and reverse, each with 64 LSTM units; Layer 2 also has two LSTM layers, each with 32 LSTM units; The parameter of the repeat vector is 2; The network structures of the encoder and decoder are symmetrical about the repeat vector layer. Hence, layers 3 and 4 are same as layers 2 and 1, respectively. The last layer is the time distributed layer, which contains 200 neurons. The optimizer for training is Adam; the loss function is MAE; the batch size is 32; the dropout rate is 0.1, and the epoch number is 500.

A BSLTM AE classifier is obtained by choosing a reasonable reconstruction error as the threshold for classifying positive and negative sequences. As shown in Fig. 13, we measure the classifier's accuracy, balanced accuracy, and F1 score under different thresholds. We notice that these three values increase first and then decrease in the interval $[0.01, 0.03]$. When $\mathcal{L} = \mathcal{L}_T = 0.019$, its accuracy, balanced accuracy, and F1 score achieve maximum values. Therefore, \mathcal{L}_T is chosen as the threshold of the classifier.

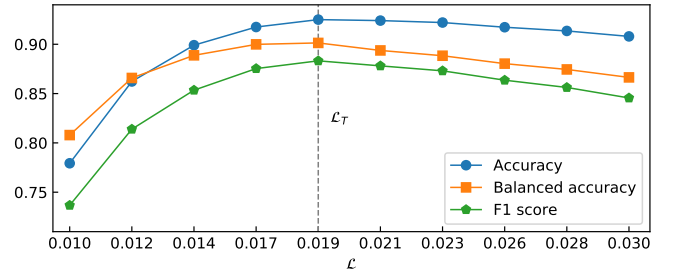


FIG. 13. The accuracy, balanced accuracy, and F1 score of the BLSTM autoencoder classifier in the testing data at different reconstruction error thresholds. The reconstruction error $\mathcal{L}_T = 0.019$ is chosen as the threshold for the BLSTM autoencoder classifier corresponding to the highest values of the accuracy, balanced accuracy, and F1 score.

SUPPLEMENTARY MATERIAL

See supplementary material for the typical DA exchange and diffusion processes in bulk water. Video 1 (DA1_09_14.mp4): A typical DA exchange process in bulk water; Video 2 (DF2_23_35.mp4): A typical diffusion process in bulk water)

ACKNOWLEDGMENTS

This research was supported by the National Natural Science Foundation of China (NSFC) (Grant Nos. 21973070). The simulations were performed on the cluster in the College of Mathematics and Physics at Wenzhou University.

Appendix A: Classification demonstrations

Figure 14 shows different types of dynamic processes of H-bond configuration. We can classify those processes by looking at the O-O distance and angles. (A), (B), and (C) are DA exchanges; (D), (E), and (F) are diffusions; (G), (H), and (I) are negative processes. \tilde{h}_s is the normalized result of \tilde{h} ; \tilde{h}_f is the filtered \tilde{h}_s ; \tilde{h}_r is the sequence reconstructed by the BLSTM AE. We see that the \tilde{h}_r and \tilde{h}_f of DA exchange and diffusion sequences almost coincide, which means the BLSTM AE can reconstruct DA exchange and diffusion sequences very well. However, the \tilde{h}_f of negative sequences can not be reconstructed well. Finally, the positive sequences are inputted into the final classifier; and the range δ of \tilde{h}_f is used to determine whether the sequence is DA exchange or diffusion. Figure 15 shows the reconstruction errors and ranges corresponding to different \tilde{h} sequences in Fig. 14. The background colors represent the predictions of the BLSTM AE classifier. Red, blue, and green denote the DA exchange, diffusion, and negative process, respectively, indicating that the BLSTM AE classifier can correctly classify the H-bond configuration change processes.

Appendix B: Step size effect of the sliding window

Since we use the sliding window method for sampling the dynamic trajectory of \tilde{h} to obtain the 8 ps sequences, we take the sliding step as a parameter to observe the relative ratios of DA exchange and diffusion processes. As shown in Fig. 16, we find that this relative ratio is almost unaffected by the step size of the sliding window.

DATA AVAILABILITY STATEMENT

The data that support the findings of this study are available from the corresponding author upon reasonable request.

- ¹D. Kennedy, "What don't we know?" *Science* **309**, 75–75 (2005).
- ²F. Franks, *Water: a matrix of life*, 2nd ed. (Royal Society of Chemistry, 2000).
- ³S. K. Pal and A. H. Zewail, "Dynamics of water in biological recognition," *Chemical Reviews* **104**, 2099–2124 (2004).
- ⁴M. Chaplin, "Do we underestimate the importance of water in cell biology?" *Nature Reviews Molecular Cell Biology* **7**, 861–866 (2006).
- ⁵P. Ball, "Water is an active matrix of life for cell and molecular biology," *Proceedings of the National Academy of Sciences* **114**, 13327–13335 (2017).
- ⁶F. H. Stillinger, "Water revisited," *Science* **209**, 451–457 (1980).
- ⁷J. R. Errington and P. G. Debenedetti, "Relationship between structural order and the anomalies of liquid water," *Nature* **409**, 318–321 (2001).
- ⁸I. Dumé, "Second critical point appears in two models of water," *Physics World* **33**, 7i–7i (2020).
- ⁹R. Kumar, J. R. Schmidt, and J. L. Skinner, "Hydrogen bonding definitions and dynamics in liquid water," *The Journal of Chemical Physics* **126**, 204107 (2007).
- ¹⁰A. Nilsson and L. G. M. Pettersson, "The structural origin of anomalous properties of liquid water," *Nature Communications* **6** (2015), 10.1038/ncomms9998.
- ¹¹U. Wilhelmsen and D. Deutsches Elektronen-Synchrotron, *The strangest liquid in the world: water amazes scientists time and again*, edited by

- T. Mundzeck, Vol. 20 (Deutsches Elektronen Synchrotron, DESY, Hamburg, 2020) p. 44 pages.
- ¹²A. Luzar and D. Chandler, "Hydrogen-bond kinetics in liquid water," *Nature* **379**, 55–57 (1996).
- ¹³E. T. Karamatskos, S. Raabe, T. Mullins, A. Trabattani, P. Stammer, G. Goldsztejn, R. R. Johansen, K. Dlugolecki, H. Stapelfeldt, M. J. J. Vrakking, S. Trippel, A. Rouzée, and J. Küpper, "Molecular movie of ultrafast coherent rotational dynamics of OCS," *Nature Communications* **10** (2019), 10.1038/s41467-019-11122-y.
- ¹⁴F. Perakis, G. Camisasca, T. J. Lane, A. Späh, K. T. Wikfeldt, J. A. Sellberg, F. Lehmkuhler, H. Pathak, K. H. Kim, K. Amann-Winkel, S. Schreck, S. Song, T. Sato, M. Sikorski, A. Eilert, T. McQueen, H. Ogasawara, D. Nordlund, W. Roseker, J. Koralek, S. Nelson, P. Hart, R. Alonso-Mori, Y. Feng, D. Zhu, A. Robert, G. Grübel, L. G. M. Pettersson, and A. Nilsson, "Coherent x-rays reveal the influence of cage effects on ultrafast water dynamics," *Nature Communications* **9** (2018), 10.1038/s41467-018-04330-5.
- ¹⁵T. Mitsui, "Water diffusion and clustering on pd(111)," *Science* **297**, 1850–1852 (2002).
- ¹⁶T. Kumagai, M. Kaizu, S. Hatta, H. Okuyama, T. Aruga, I. Hamada, and Y. Morikawa, "Direct observation of hydrogen-bond exchange within a single water dimer," *Physical Review Letters* **100** (2008), 10.1103/physrevlett.100.166101.
- ¹⁷H. J. Bakker and H.-K. Nienhuys, "Delocalization of protons in liquid water," *Science* **297**, 587–590 (2002).
- ¹⁸C. J. Fecko, "Ultrafast hydrogen-bond dynamics in the infrared spectroscopy of water," *Science* **301**, 1698–1702 (2003).
- ¹⁹K. ichi Inoue, M. Ahmed, S. Nihonyanagi, and T. Tahara, "Reorientation-induced relaxation of free OH at the air/water interface revealed by ultrafast heterodyne-detected nonlinear spectroscopy," *Nature Communications* **11** (2020), 10.1038/s41467-020-19143-8.
- ²⁰T. Iwashita, B. Wu, W.-R. Chen, S. Tsutsui, A. Q. R. Baron, and T. Egami, "Seeing real-space dynamics of liquid water through inelastic x-ray scattering," *Science Advances* **3**, e1603079 (2017).
- ²¹Z.-H. Loh, G. Doumy, C. Arnold, L. Kjellsson, S. H. Southworth, A. A. Haddad, Y. Kumagai, M.-F. Tu, P. J. Ho, A. M. March, R. D. Schaller, M. S. B. M. Yusuf, T. Debnath, M. Simon, R. Welsch, L. Inhester, K. Khalili, K. Nanda, A. I. Krylov, S. Moeller, G. Coslovich, J. Koralek, M. P. Minitti, W. F. Schlotter, J.-E. Rubensson, R. Santra, and L. Young, "Observation of the fastest chemical processes in the radiolysis of water," *Science* **367**, 179–182 (2020).
- ²²T. Head-Gordon and G. Hura, "Water structure from scattering experiments and simulation," *Chemical Reviews* **102**, 2651–2670 (2002).
- ²³V. A. Ranea, A. Michaelides, R. Ramírez, P. L. de Andres, J. A. Vergés, and D. A. King, "Water dimer diffusion on pd{111} assisted by an h-bond donor-acceptor tunneling exchange," *Physical Review Letters* **92** (2004), 10.1103/physrevlett.92.136104.
- ²⁴D. Laage and J. T. Hynes, "A Molecular Jump Mechanism of Water Reorientation," *Science* **311**, 832–835 (2006).
- ²⁵W. Fang, J. Chen, P. Pedevilla, X.-Z. Li, J. O. Richardson, and A. Michaelides, "Origins of fast diffusion of water dimers on surfaces," *Nature Communications* **11** (2020), 10.1038/s41467-020-15377-8.
- ²⁶R. S. Fellers, C. Leforestier, L. B. Braly, M. G. Brown, and R. J. Saykally, "Spectroscopic determination of the water pair potential," *Science* **284**, 945–948 (1999).
- ²⁷F. N. Keutsch and R. J. Saykally, "Water clusters: Untangling the mysteries of the liquid, one molecule at a time," *Proceedings of the National Academy of Sciences* **98**, 10533–10540 (2001).
- ²⁸N. Agmon, "The grothuss mechanism," *Chemical Physics Letters* **244**, 456–462 (1995).
- ²⁹J. L. Thomaston, R. A. Woldeyes, T. Nakane, A. Yamashita, T. Tanaka, K. Koiwai, A. S. Brewster, B. A. Barad, Y. Chen, T. Lemmin, M. Uervirojnangkoorn, T. Arima, J. Kobayashi, T. Masuda, M. Suzuki, M. Sugahara, N. K. Sauter, R. Tanaka, O. Nureki, K. Tono, Y. Joti, E. Nango, S. Iwata, F. Yumoto, J. S. Fraser, and W. F. DeGrado, "XFEL structures of the influenza m2 proton channel: Room temperature water networks and insights into proton conduction," *Proceedings of the National Academy of Sciences* **114**, 13357–13362 (2017).
- ³⁰M. D. Gelenter, V. S. Mandala, M. J. M. Niesen, D. A. Sharon, A. J. Dregni, A. P. Willard, and M. Hong, "Water orientation and dynamics in the closed

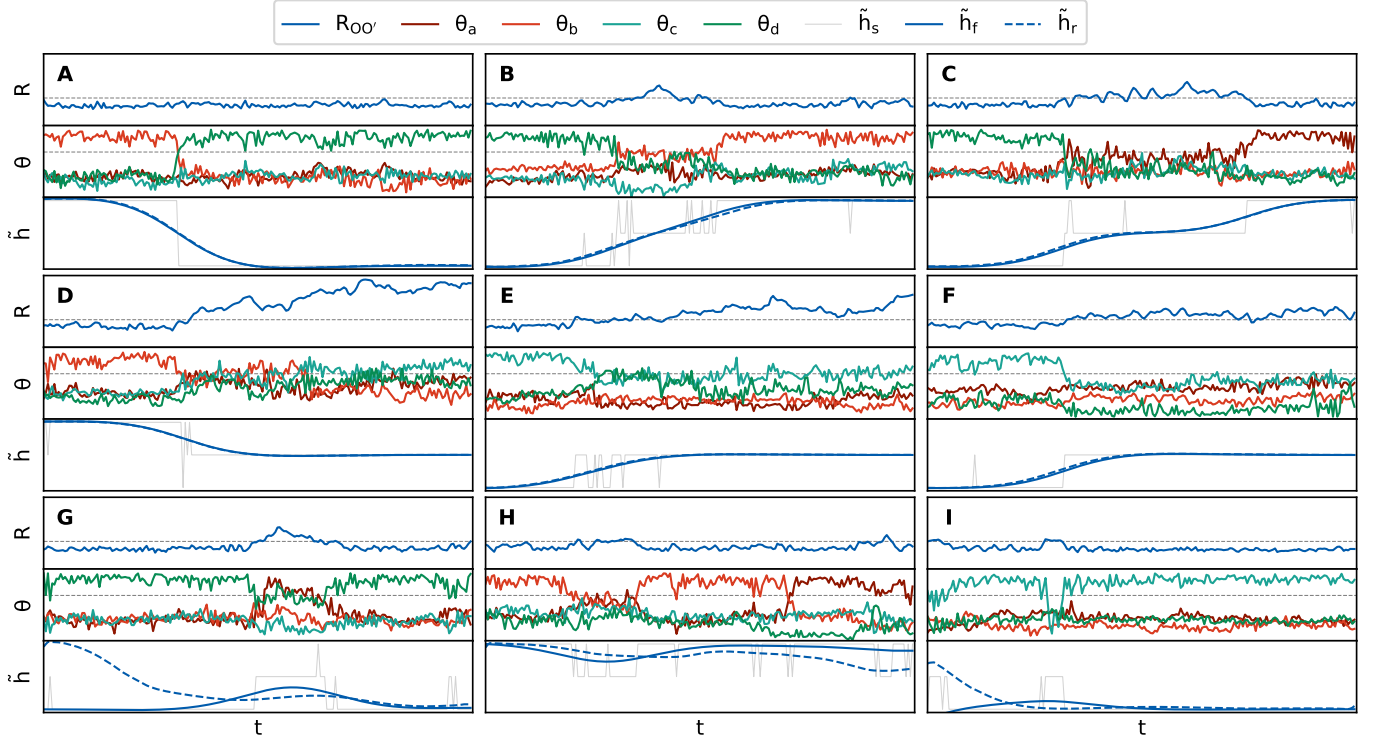


FIG. 14. Different types of H-bond configuration change processes. (A), (B), and (C) are DA exchange processes; (D), (E), and (F) are diffusion processes; (G), (H), and (I) are negative processes. The corresponding simulation time for each sequence is 8 ps.

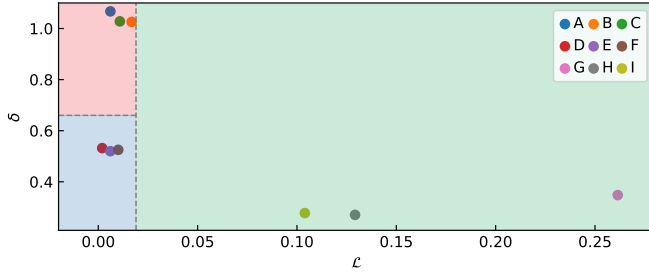


FIG. 15. Classification results for sequences in Fig. 14.

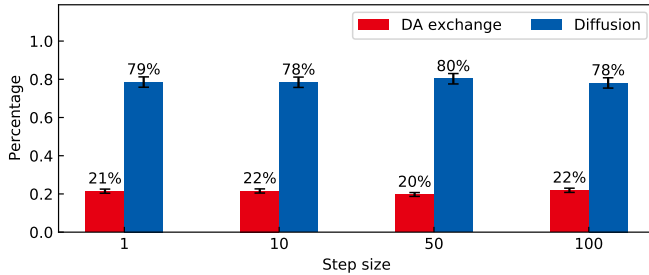


FIG. 16. The relative ratios of DA exchange and diffusion processes under different step sizes for the simulation bulk water at 310 K.

and open influenza b virus m2 proton channels," *Communications Biology* **4**, 338 (2021).

- ³¹T. D. Kühne, M. Iannuzzi, M. D. Ben, V. V. Rybkin, P. Seewald, F. Stein, T. Laino, R. Z. Khaliullin, O. Schütt, F. Schiffmann, D. Golze, J. Wilhelm, S. Chulkov, M. H. Bani-Hashemian, V. Weber, U. Borštnik, M. Tailliefumier, A. S. Jakobovits, A. Lazzaro, H. Pabst, T. Müller, R. Schade, M. Guidon, S. Andermatt, N. Holmberg, G. K. Schenter, A. Hehn, A. Bussy, F. Belleflamme, G. Tabacchi, A. Glöb, M. Lass, I. Bethune, C. J. Mundy, C. Plessl, M. Watkins, J. VandeVondele, M. Krack, and J. Hutter, "CP2k: An electronic structure and molecular dynamics software package - quickstep: Efficient and accurate electronic structure calculations," *The Journal of Chemical Physics* **152**, 194103 (2020).
- ³²D. E. Moilanen, D. Wong, D. E. Rosenfeld, E. E. Fenn, and M. D. Fayer, "Ion-water hydrogen-bond switching observed with 2d ir vibrational echo chemical exchange spectroscopy," *Proceedings of the National Academy of Sciences* **106**, 375–380 (2009).
- ³³M. Ji, M. Odellius, and K. J. Gaffney, "Large angular jump mechanism observed for hydrogen bond exchange in aqueous perchlorate solution," *Science* **328**, 1003–1005 (2010).
- ³⁴R. Schulz, Y. von Hansen, J. O. Daldrop, J. Kappler, F. Noé, and R. R. Netz, "Collective hydrogen-bond rearrangement dynamics in liquid water," *The Journal of Chemical Physics* **149**, 244504 (2018).
- ³⁵E. Méndez and D. Laria, "Nuclear quantum effects on the hydrogen bond donor-acceptor exchange in water-water and water-methanol dimers," *The Journal of Chemical Physics* **153**, 054302 (2020).
- ³⁶F. Sciortino and S. L. Fornili, "Hydrogen bond cooperativity in simulated water: Time dependence analysis of pair interactions," *The Journal of Chemical Physics* **90**, 2786–2792 (1989).
- ³⁷S. Balasubramanian, S. Pal, and B. Bagchi, "Hydrogen-bond dynamics near a micellar surface: Origin of the universal slow relaxation at complex aqueous interfaces," *Physical Review Letters* **89** (2002), 10.1103/physrevlett.89.115505.
- ³⁸N. Michaud-Agrawal, E. J. Denning, T. B. Woolf, and O. Beckstein, "MD-Analysis: A toolkit for the analysis of molecular dynamics simulations," *Journal of Computational Chemistry* **32**, 2319–2327 (2011).
- ³⁹T. W. Hughes, I. A. D. Williamson, M. Minkov, and S. Fan, "Wave physics as an analog recurrent neural network," *Science Advances* **5** (2019),

- 10.1126/sciadv.aay6946.
- ⁴⁰N. Rank, B. Pfahringer, J. Kempfert, C. Stamm, T. Kühne, F. Schoenrath, V. Falk, C. Eickhoff, and A. Meyer, “Deep-learning-based real-time prediction of acute kidney injury outperforms human predictive performance,” *npj Digital Medicine* **3** (2020), 10.1038/s41746-020-00346-8.
 - ⁴¹S.-T. Tsai, E.-J. Kuo, and P. Tiwary, “Learning molecular dynamics with simple language model built upon long short-term memory neural network,” *Nature Communications* **11** (2020), 10.1038/s41467-020-18959-8.
 - ⁴²J. J. Hopfield, “Neural networks and physical systems with emergent collective computational abilities,” *Proceedings of the National Academy of Sciences* **79**, 2554–2558 (1982).
 - ⁴³S. Hochreiter and J. Schmidhuber, “Long short-term memory,” *Neural Computation* **9**, 1735–1780 (1997).
 - ⁴⁴R. Z. Khaliullin and T. D. Kühne, “Microscopic properties of liquid water from combined ab initio molecular dynamics and energy decomposition studies,” *Phys. Chem. Chem. Phys.* **15**, 15746–15766 (2013).
 - ⁴⁵T. D. Kühne, M. Krack, F. R. Mohamed, and M. Parrinello, “Efficient and accurate car-parrinello-like approach to born-oppenheimer molecular dynamics,” *Physical Review Letters* **98** (2007), 10.1103/physrevlett.98.066401.
 - ⁴⁶M. Krack and M. Parrinello, “All-electron ab-initio molecular dynamics,” *Physical Chemistry Chemical Physics* **2**, 2105–2112 (2000).
 - ⁴⁷J. D. Smith, C. D. Cappa, K. R. Wilson, R. C. Cohen, P. L. Geissler, and R. J. Saykally, “Unified description of temperature-dependent hydrogen-bond rearrangements in liquid water,” *Proceedings of the National Academy of Sciences* **102**, 14171–14174 (2005).
 - ⁴⁸S. Garrett-Roe and P. Hamm, “The oh stretch vibration of liquid water reveals hydrogen-bond clusters,” *Physical Chemistry Chemical Physics* **12**, 11263–11266 (2010).
 - ⁴⁹J. VandeVondele, M. Krack, F. Mohamed, M. Parrinello, T. Chassaing, and J. Hutter, “Quickstep: Fast and accurate density functional calculations using a mixed gaussian and plane waves approach,” *Comput. Phys. Commun.* **167**, 103–128 (2005).
 - ⁵⁰A. D. Becke, “Density-functional exchange-energy approximation with correct asymptotic behavior,” *Phys. Rev. A* **38**, 3098 (1988).
 - ⁵¹C. Lee, W. Yang, and R. G. Parr, “Development of the colic-salvetti correlation-energy formula into a functional of the electron density,” *Phys. Rev. B* **37**, 785 (1988).
 - ⁵²C. Hartwigsen, S. Goedecker, and J. Hutter, “Relativistic separable dual-space gaussian pseudopotentials from H to Rn,” *Phys. Rev. B* **58**, 3641–3662 (1998).
 - ⁵³J. H. G. Lippert and M. Parrinello, “The gaussian and augmented-plane-wave density functional method for ab initio molecular dynamics simulations,” *Theor. Chem. Acc.* **103**, 124 (1999).
 - ⁵⁴J. VandeVondele and J. Hutter, “Gaussian basis sets for accurate calculations on molecular systems in gas and condensed phases,” *The Journal of Chemical Physics* **127**, 114105 (2007).
 - ⁵⁵G. J. Martyna, M. L. Klein, and M. Tuckerman, “Nosé-hoover chains: The canonical ensemble via continuous dynamics,” *J. Chem. Phys.* **97**, 2635 (1992).
 - ⁵⁶S. Grimme, J. Antony, S. Ehrlich, and H. Krieg, “A Consistent and Accurate Ab Initio Parametrization of Density Functional Dispersion Correction (DFT-D) for the 94 Elements H-Pu,” *J. Chem. Phys.* **132**, 154104 (2010).
 - ⁵⁷P. Virtanen, R. Gommers, T. E. Oliphant, M. Haberland, T. Reddy, D. Cournapeau, E. Burovski, P. Peterson, W. Weckesser, J. Bright, S. J. van der Walt, M. Brett, J. Wilson, K. J. Millman, N. Mayorov, A. R. J. Nelson, E. Jones, R. Kern, E. Larson, C. J. Carey, Í. Polat, Y. Feng, E. W. Moore, J. VanderPlas, D. Laxalde, J. Perktold, R. Cimrman, I. Henriksen, E. A. Quintero, C. R. Harris, A. M. Archibald, A. H. Ribeiro, F. Pedregosa, and P. van Mulbregt, “SciPy 1.0: fundamental algorithms for scientific computing in python,” *Nature Methods* **17**, 261–272 (2020).
 - ⁵⁸A. Graves, M. Liwicki, S. Fernandez, R. Bertolami, H. Bunke, and J. Schmidhuber, “A novel connectionist system for unconstrained handwriting recognition,” *IEEE Transactions on Pattern Analysis and Machine Intelligence* **31**, 855–868 (2009).
 - ⁵⁹M. Schuster and K. Paliwal, “Bidirectional recurrent neural networks,” *IEEE Transactions on Signal Processing* **45**, 2673–2681 (1997).
 - ⁶⁰P. Baldi, S. Brunak, P. Frasconi, G. Soda, and G. Pollastri, “Exploiting the past and the future in protein secondary structure prediction,” *Bioinformatics* **15**, 937–946 (1999).